

Meeting Experiments at the Diffraction Barrier with *In-silico* Fluorescence Microscopy

Subhamoy Mahajan and Tian Tang*

Department of Mechanical Engineering, University of Alberta, Edmonton, AB T6G 1H9, Canada

*Corresponding author, Email: tian.tang@ualberta.ca

Abstract

Fluorescence microscopy allows the visualization of live-cells and their components, but even with advances in super-resolution microscopy, atomic resolution remains unattainable. Contrarily, molecular simulations can access atomic resolution, but comparison with experimental microscopy images has not been possible. In this work, a novel *in-silico* fluorescence microscopy technique is proposed, which uses physics-based point-spread-function to generate images from molecular simulations. The method allows the resolution of molecular simulation to be reduced and made comparable to experiments, enabling direct cross-comparison between *in-silico* and experimental images. Simulation of a DNA-polyethylenimine gene delivery system is used to demonstrate the production of *in-silico* images with a different optical axis, object focal planes, exposure time, color combinations, resolution, brightness, and amount of out-of-focus fluorescence. These images bridge the distinct worlds of molecular simulation and experimental fluorescence microscopy by generating new knowledge from direct cross-validation, determining equivalence of properties extracted from molecular simulation and experimental images, assessing and developing algorithms for experimental image analysis, *etc.* The technique presented here can also be used as a standalone visualization tool for molecular simulation and lays the foundation for other *in-silico* microscopy methods.

Keywords: Molecular simulation; *In-silico* fluorescence microscopy; Software and online tools; Hue-saturation-value color mixing; Fluorescence correlation spectroscopy; Photophysical process

Microscopy has enabled the exploration of tissues, cells, and its components,¹⁻³ structure and properties of biochemicals,⁴⁻⁶ surface properties of materials,^{7,8} and advances in many other fields. Fluorescence microscopy accounting for more than eighty percent of all microscopy images,⁹ has enabled qualitative and quantitative analysis of live-cell processes.¹⁰ Such analysis includes, but is not limited to the fluorophores' colocalization,¹¹⁻¹³ intensity,¹⁴⁻¹⁶ count,^{12,14} diameter,¹² area,¹⁷ volume,¹¹ shape,¹⁴ mean-squared displacement (MSD),¹² position,^{11,12,18} diffusion,^{12,15} speed,¹¹ *etc.*, which form a key understanding of various biological processes. Excellent reviews on different fluorescence microscopy techniques and their applications can be found in Schermelleh *et al.*,¹⁹ Sahl *et al.*,²⁰ Lichtman and Conchello,²¹ Stephens and Allan,²² and Huang *et al.*¹

The intrinsic limitation of fluorescence microscopy arises due to diffraction,²³ which is quantified by the effective point-spread-function (PSF) of a microscope. Standard fluorescence microscopy, such as widefield, experiences the resolution limit (i.e., diffraction barrier) of ~200 nm in the lateral direction when imaging cells because only visible spectra can be used to avoid photodamage to the cells.^{10,23} The images also suffer from a further reduction in resolution due to the detection of out-of-focus fluorescence. Like widefield, optical sectioning microscopy (OSM) techniques such as confocal,²⁴ light-sheet,²⁵ two-photon,²⁶ *etc.* are also diffraction-limited, but they improve the resolution of images by reducing the amount of out-of-focus fluorescence. Computational optical-sectioning microscopy (COSM) can be used, on a stack of 2D images obtained from different object focal planes (i.e., an equivalent 3D image), to further reduce the amount of out-of-focus fluorescence.^{27,28} This is achieved by applying theoretical or experimental knowledge of the microscope's PSF and certain deconvolution algorithms.^{28,29} COSM can also be used directly on 2D images and those obtained from widefield microscopy. Even with advances in OSM and COSM observing fine details in most cellular organelles seemed impossible until a few decades ago. Innovations in the field of super-resolution microscopy³⁰⁻³⁴ have broken the

traditional diffraction barrier to achieve resolution as low as 20 nm. However, atomistic resolution on the order of angstroms still remains out of reach in fluorescence microscopy.

On the other hand, molecular simulations (MS) can probe biochemical systems with molecular,³⁵ sub-molecular,^{36,37} or atomic³⁸ resolutions. Here for the first time, we present a generalized framework for performing *in-silico* fluorescence microscopy on a virtual specimen represented by MS trajectories. Different types of *in-silico* fluorescence microscopy can be achieved, and the wide and versatile applications of the method are demonstrated. It is critical to mention that in the literature the term “computational microscopy” refers to either a collection of MS not at all linked to microscopy,^{39,40} or computational techniques applied on microscopy images to improve their quality and therefore not related to MS.^{41,42} The framework proposed here is also distinct from existing studies in the literature that modeled microscopes, which focused on developing different PSFs to more accurately extract information from microscopy images.^{43–46} Since the development of COSM,^{27,28} synthetic microscopy images have been generated by convoluting number density of objects placed in 2D or 3D space (considered “ground truth”) with a PSF to test analysis tools in experimental microscopy.^{27,47–50} As such, the “ground truth” used are not realistic and do not possess any predictive power. Much more information can be gained by bridging the worlds of physics-based MS and experimental fluorescence microscopy. In this regard, Dix *et al.*⁵¹ developed an *in-silico* fluorescence correlation spectroscopy (FCS), a statistical technique to analyze temporal fluctuations of fluorescence intensity in a control volume. The technique was applied to a Brownian dynamics simulation where the fluorophores were modeled as simple particles. Angiolini *et al.*⁵² developed a similar *in-silico* FCS and fluorescence cross-correlation spectroscopy (FCCS) for a reaction-diffusion model of a cell. The *in-silico* FCS and FCCS are valuable tools because they allow the comparison of chemical kinetics, diffusion coefficients, and inter-particle interactions obtained from numerical simulations and experiments

(a review of experimental FCS and FCCS techniques is available in Macháň and Wohland⁵³). However, the work by Dix *et al.*⁵¹ and Angiolini *et al.*⁵² lacked spatial resolution which is present in images or videos. Watabe *et al.*⁵⁴ and Lindén *et al.*⁵⁵ generated microscopy images for reaction-diffusion models of cells, and performed limited comparison (e.g. single-particle tracking) with experiments. While reaction-diffusion models are useful, unlike MS they are incapable of predicting molecular interactions. To our knowledge, *in-silico* fluorescence microscopy performed on MS with detailed molecular interactions and structures is still absent in the literature.

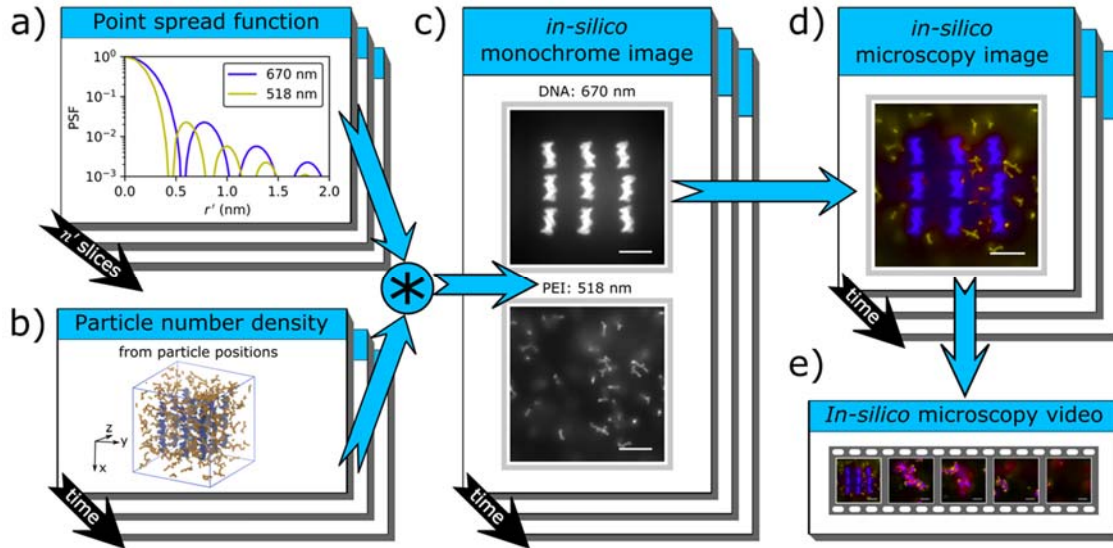


Figure 1. A framework of *in-silico* microscopy. (a) PSF with $I_0 = 1$, $\beta = 59.4^\circ$, $\mu = 1.51$, $P_l' = P_m' = P_n' = 25$ nm, $\Delta l' = \Delta m' = 0.1$ nm, $\Delta n' = 0.05$ nm, $n' = 0$ nm, and $f_s = 530$ (eqn (1)). In this work, PSF is calculated for $\lambda = 461$ (not shown), 518, and 670 nm (corresponding to emission peaks of DAPI (4',6-diamidino-2-phenylindole), FITC (Fluorescein isothiocyanate), and Cy5 (Cyanine 5)) at different n' (black arrow). (b) To highlight the features of the framework, a polyethylenimine (PEI)-DNA aggregation simulation³⁶ (see Methods) is used as an MS specimen where PEI and DNA particles are assumed to emit fluorescence. The box represents the initial configuration of the MS, in the xyz coordinate system shown. DNAs are shown in blue and PEIs in orange. Particles in DNA and PEI molecules are assigned two different fluorophore types and their number density (ρ) is calculated based on their positions, at different simulation times (black arrow). (c) *In-silico* monochrome images for DNA (top) and PEI (bottom) are obtained (at different simulation times; black arrow) using the convolution (*) between PSF specified in (a) and ρ (eqn (2)). In the images shown, $t = 0$, n is taken to be the z -axis and the object focal plane is at $n_O = 12$ nm. DNA and PEI particles emit light with $(\lambda, I_0) = (670$ nm, 0.13) and (518 nm, 0.27) respectively. Bright-white and dim-diffused-white colors represent in-focus and out-of-focus fluorescence respectively. (d) A colored *in-silico* microscopy image is generated by assigning indigo hue to the top figure in (c) and yellow hue to the bottom figure in (c), and colors are mixed in the hue-saturation-value space using eqn (3-5). (e) Microscopy images generated at different simulation times can be combined into a microscopy video. Scale bars in (c-e), 5 nm.

The *in-silico* fluorescence microscopy created in this work can achieve functionalities similar to experimental fluorescence microscopies. As an example, widefield fluorescence microscopy follows simple optics, where the entire specimen is illuminated, imaging fluorescence from both in- and out-of-focus. Fluorophores with different emission peaks can be detected using one or multiple cameras.⁵⁶ While both color and monochrome cameras are available, monochrome cameras are often used because of their higher sensitivity and resolution.⁵⁶ Artificial colors can be digitally assigned to the monochrome images and superimposed to produce a colored microscopy image.⁵⁷ Images (monochrome or colored) taken at different times can be combined to form a microscopy video, to examine the temporal variations in the locations of different fluorophores and their colocalization. The optics of OSM is similar to widefield, where a thin optical section around the object focal plane is illuminated instead of the entire specimen and/or most of the out-of-focus fluorescence is blocked using an aperture. Similarly, the optics of some super-resolution microscopies such as stimulated emission depletion³¹ (STED) microscopy resembles that of widefield but with a lower effective emission wavelength leading to higher resolution.⁵⁸

Analogous principles are followed in the *in-silico* fluorescence microscopy with the additional advantage of tunable resolution and amount of out-of-focus fluorescence. Detailed particle positions from an MS and PSF are used to generate fluorescence intensities, turning an MS “specimen” into *in-silico* monochrome images/videos, which are then superimposed with different hues to form colored *in-silico* microscopy images/videos (**Figure 1**). MS and experimental microscopy calculate physical properties using different principles, but they can now be directly compared through the *in-silico* images/videos. Since precise positions of particles are known through MS (the ground truth), a direct link between the position/motion of particles (**Figure 1b**) and *in-silico* microscopy images/videos (**Figure 1c-e**) can be established. This will not only allow cross-validation between experiments and MS, but also aid in the understanding of subcellular

processes and mechanisms by combining knowledge from MS and experiments which may cover different length and time scales. Three-dimensional MS trajectories, although containing a large amount of quantitative information, are tedious (if not difficult) to view and analyze on a two-dimensional screen. The *in-silico* fluorescence microscopy presented here aims to provide a novel easy-to-use open-source visualization toolbox, which allows researchers to observe more by reducing the quantitative details.

Results

Setup of the *in-silico* microscope. A linear and lateral shift-invariant *in-silico* microscope (\mathcal{L}) is set up to observe an MS specimen (\mathcal{MS}) with an arbitrarily chosen right-handed rectangular coordinate system lmn , where lm forms the lateral plane and n is the optical axis (**Figure 2**). The microscope is focused on the object focal plane (\mathcal{F}_O in **Figure 2**) where $n = n_o$. Selected microscopy images generated with different n -axis and n_o are shown in **Figure 3a**. For a given lmn , images taken at different n_o provide insight into the 3D structure of the \mathcal{MS} .

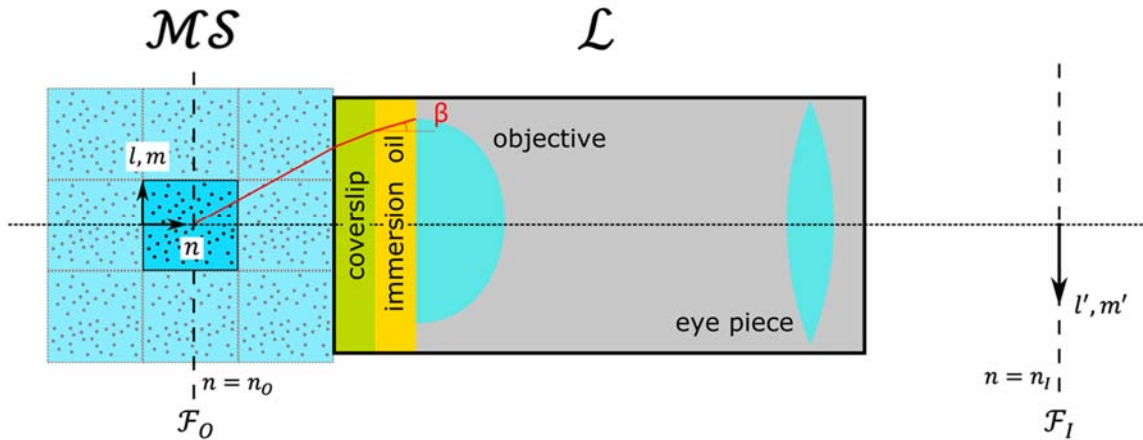


Figure 2. Schematic of the *in-silico* microscope. \mathcal{MS} is the MS specimen being viewed under the *in-silico* microscope \mathcal{L} . The central box in \mathcal{MS} is the original MS system, and the adjacent boxes with equal dimensions to the original MS system are its periodic images if periodic boundary condition is applied. \mathcal{L} consists of a virtual cover slip, immersion oil, objective lens, and eyepiece. lmn is a right-handed coordinate system of the MS, where n is the optical axis. \mathcal{F}_O and \mathcal{F}_I are the object and image focal planes respectively. The object focal plane is located at $n = n_o$ and the image focal plane at $n = n_i$.

The image of \mathcal{MS} is produced in the image focal plane $n = n_I$ (\mathcal{F}_I in **Figure 2**), magnifying the \mathcal{MS} coordinates by $-M$; i.e., in-focus fluorophore particle with coordinates (l_j, m_j, n_O) produces a focal spot at $(-Ml_j, -Mm_j, n_I)$. An image coordinate system $l'm'$ is introduced which scales the lm coordinates by $-1/M$, such that the image coordinates of the focal spot $(-Ml_j, -Mm_j, n_I)$ are given by $(l', m') = \left(\frac{-Ml_j}{-M}, \frac{-Mm_j}{-M}\right) = (l_j, m_j)$. Fluorophore particles in \mathcal{MS} , both in- and out-of-focus, each generate an intensity profile around its own focal spot, which is characterized by the PSF. For the *in-silico* microscope with an ideal aberration-free high-magnification objective lens, the PSF is modeled using eqn (1).⁴⁴

$$PSF(r', n') \equiv PSF(l', m', n', \lambda) = I_0 \left| \frac{3}{2(1 - \cos^{3/2} \beta)} \int_0^\beta e^{-ik'\mu n' \cos \theta} J_0(k'\mu r' \sin \theta) \sin \theta \cos^{1/2} \theta d\theta \right|^2 \quad (1)$$

Eqn (1) describes the intensity produced at a point (l', m') in \mathcal{F}_I by a fluorophore particle located at $(0, 0, n_O - n')$, a distance of n' away from \mathcal{F}_O . $r' = \sqrt{(l')^2 + (m')^2}$, i is the unit imaginary number, and J_0 is zeroth-order Bessel function of the first kind. The wavenumber $k' = 2\pi f_s / \lambda$, where λ is the wavelength of the emitted light in vacuum, which is 461, 518, and 670 nm respectively for fluorophores DAPI (4',6-diamidino-2-phenylindole), FITC (Fluorescein isothiocyanate), and Cy5 (Cyanine 5), and f_s a scaling factor introduced to tune the full-width-at-half-maximum (FWHM). I_0 is the maximum PSF intensity, $\beta = \sin^{-1}(\text{NA}/\mu)$ the maximum half-angle in the virtual immersion oil (**Figure 2**), NA the numerical aperture of the virtual objective lens, and μ the refractive index of the virtual immersion oil. The factor $3/2(1 - \cos^{3/2} \beta)$ is a normalization constant to ensure the maximum of PSF is I_0 for $n' = 0$.⁴⁴ In this form of the PSF, Gandy⁴⁴ assumed that the microscope is in design condition and the effective refractive index of the specimen is comparable to the immersion oil, which makes the PSF depth-invariant. Because of this, the location of the object plane (n_O) does not explicitly appear in eqn (1). The location of the image focal plane (n_I) also does not appear in eqn (1) because for a microscope, n_I solely depends on the design parameters (focal

length of objective, eyepiece, thickness of coverslip and immersion oil, tube length, *etc.*) and its effect is felt through the magnification M . For example, magnification in a simplified microscope with only an objective lens is given by the ratio between the distances of the image and object from the objective lens. Since the microscope is linear and lateral shift-invariant, the PSF defined for a fluorophore particle at $(0, 0, n_o - n')$ can be used to calculate the contribution of particles located elsewhere by a simple shift operation. It is worth noting that the *in-silico* microscope presented in this work is not limited to the PSF given in eqn (1). Other PSF available in the literature, such as those proposed by Gibson and Lanni,⁴³ Hell *et al.*,⁴⁶ can also be used. More discussions on this are given in supporting information (SI) Section S1.

For computational efficiency, $PSF(l', m', n', \lambda)$ is predetermined with $I_0 = 1$ at grid points within a cuboidal box that has a dimension of (P_l', P_m', P_n') and constant grid spacing of $\Delta l'$, $\Delta m'$ and $\Delta n'$. Typical PSF curves are shown in **Figure 1a**. Increasing f_s will increase k' , which is equivalent to decreasing λ , compressing the PSF along the r' axis (**Figure 1a**) and reducing the “spread” of the fluorescence intensity. This effectively decreases the FWHM making the *in-silico* microscopy images sharper (**Figure 3b**) and can be used to model super-resolution microscopy (See SI Section S2). Increasing I_0 elongates the PSF along the vertical axis, causing the intensity of some local maxima in the PSF (**Figure 1a**) to exceed the minimum detection threshold of human vision. This makes the *in-silico* microscopy images brighter while increasing the radial distance over which each fluorophore particle contributes to the resultant image (**Figure 3c**). A concise guide on how to choose f_s and I_0 is available in SI Section S3. $P_l'/2$ and $P_m'/2$ are respectively the maximum lateral distances in directions l' and m' over which the fluorescence of a particle located at $(0, 0, n_o - n')$ is calculated. In general, P_l' and P_m' should be large enough such that the PSF decays to zero within the box of dimension (P_l', P_m') . $P_n'/2$ is the maximum distance of a fluorophore particle from \mathcal{F}_O for which its fluorescence contribution is calculated, i.e., P_n' is the thickness of

the excited specimen around \mathcal{F}_O . Therefore, decreasing P_n' decreases the amount of out-of-focus fluorescence (**Figure 3d**) and can be used to model OSM (see SI Section S2).

Generating *In-silico* monochrome image. Particles in an MS are assigned to different fluorophore types, each emitting light at a specific wavelength λ . For each fluorophore type, the resultant fluorophore intensity I detected at \mathcal{F}_I , when the object focal plane is at n_o , is calculated as the convolution between PSF (given n -axis, n_o , β , f_s , λ , and I_0) and particle number density $\rho(l, m, n, t) = \sum_{j=1}^N \delta(l - l_j(t), m - m_j(t), n - n_j(t))$ using eqn (2). The coordinates $(l_j(t), m_j(t), n_j(t))$ specify the position of the j^{th} fluorophore particle in the MS at time t , N is the number of fluorophore particles in the MS, and δ is the Dirac delta function. The convolution operator is responsible for the lateral shift-operation on the PSF based on the position of each fluorophore particle. Therefore, convolution of the PSF with ρ provides the resultant diffraction pattern produced by all fluorophores on the camera.

$$I(l', m', n_o, \lambda, t) = PSF(l', m', n_o, \lambda) * \rho(l, m, n, t) = \sum_{j=1}^N PSF(l' - l_j(t), m' - m_j(t), n_o - n_j(t)) \quad (2)$$

Similar to PSF , for computational efficiency I is predetermined with $I_0 = 1$ at discrete points where PSF was evaluated. I values calculated from $I_0 = 1$ are hereafter denoted by I_1 . To generate images, I_1 is scaled with the actual chosen I_0 value and any intensity above 1 is treated as 1; i.e., $I = \min\{I_0 I_1, 1\}$. When I is rendered as an image for a fluorophore type, it is referred to as the *in-silico* monochrome image. Periodic boundary condition (PBC) can be applied while calculating I . The number of periodic images that contribute to I depends on the dimension of the box (P_l , P_m , P_n) used to predetermine the PSF (see Methods). Because the size of the \mathcal{MS} can change over the course of the simulation, a white image frame larger than the \mathcal{MS} is created and the monochrome image is scaled with respect to the white image frame before being placed at its center (see Methods). This allows the comparison of images generated at different simulation times. An

example of the 3D distribution of fluorophore particles and the corresponding *in-silico* monochrome images are shown in **Figure 1b-c**. The white image frame is highlighted in **Figure 1c-e** by adding a grey background.

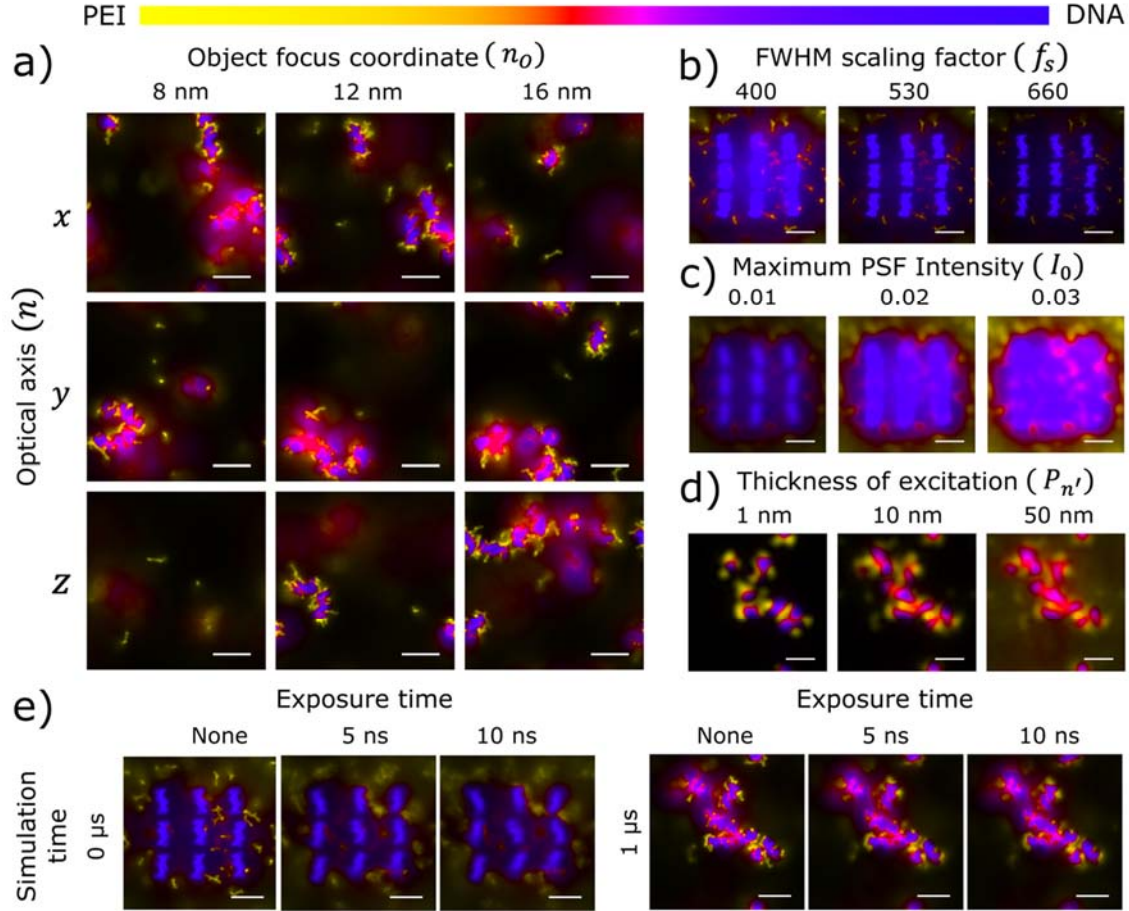


Figure 3. *In-silico* microscopy images generated with different parameters. MS on PEI-DNA aggregation³⁶ (see Methods) is used as the virtual specimen where PEI and DNA particles are assumed to emit fluorescence. Unless otherwise specified, the PSF is modeled with $\beta = 59.4^\circ$, $\mu = 1.51$, n is z -axis, $n_o = 12$ nm, $\Delta l' = \Delta m' = 0.1$ nm, $\Delta n' = 0.05$ nm, $P_l' = P_m' = P_n' = 25$ nm, $f_s = 530$, $(\lambda, I_0) = (670$ nm, 0.13) for DNA and (518 nm, 0.27) for PEI; DNA and PEI particles are assigned indigo and yellow hues respectively (colocalization color bar on the top); and no time-averaging is performed. (a) Images with different n and n_o at $t = 3$ μ s. (b) Images with different f_s , $t = 0$ μ s and $I_0 = 0.2$ for all particles. (c) Images with different I_0 at $t = 0$ μ s, $f_s = 130$. (d) Images with different P_n' at $t = 1$ μ s, $f_s = 130$. I_0 for DNA and PEI are (0.04, 0.12) (left), (0.01, 0.03) (middle), and (0.008, 0.02) (right). (e) Images with different exposure time at $t = 0$ and 1 μ s. Scale bars, 5 nm.

When generating monochrome images using Eq 2, at any time t all fluorophores are assumed to undergo the same number of light emissions for a constant time interval Δt . However, fluorophores can undergo intricate photophysical conversions between electronic states, which can

result in different number of light emissions for different fluorophores and at different time, as well as emission with different wavelengths. These photophysical conversions and emissions can be modeled by a continuous-time Markov process, to study photoblinking, photobleaching, phosphorescence, and fluorophores emitting multiple wavelengths, which is discussed in SI Section S4.

Generating In-silico microscopy image and video. The final *in-silico* microscopy image is generated by selecting a color for each monochrome image and superimposing them. The colors are mixed in the hue-saturation-value (HSV) space. Each fluorophore type is assigned a hue, saturation of 1, and value equal to $I = \min\{I_0 I, 1\}$. The hue, saturation, and value of mixed color are given by eqn (3-5), where (H_j, V_j) are the hue and value of the j^{th} color, $\arg()$ returns the phase of a complex number, and $\max_n(V_j)$ represents the n^{th} largest V_j after sorting V_j of the colors being mixed (SI Section S5). For example, if the colors being mixed have values 0.2, 0.5 and 0.5, then $\max_1(V_j) = \max_2(V_j) = 0.5$ and $\max_3(V_j) = 0.2$.

$$H_{mix} = \arg\left(\sum_{j=1}^N V_j e^{iH_j}\right) \quad (3)$$

$$V_{mix} = \max_1(V_j) \quad (4)$$

$$S_{mix} = 1 - \frac{\max_3(V_j)}{\max_1(V_j)} \quad (5)$$

For two-color mixing the third-largest V_j is zero, resulting in a fully saturated color (**Figure 4a**). When the third largest V_j is non-zero, it represents the mixing of three or more colors, and the mixed color is desaturated. A graphical representation of four-color mixing is shown in **Figure 4b**. A concise guide for choosing hues is provided in SI Section S6. A typical *in-silico* microscopy image generated from a two-color mixture of indigo (assigned to **Figure 1c**, top) and yellow (assigned to **Figure 1c**, bottom) hues is shown in **Figure 1d**.

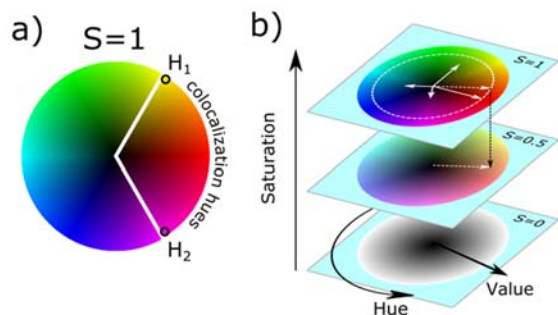


Figure 4. Demonstration of color mixing. (a) Two-color mixing always results in a fully saturated color. When hues H_1 and H_2 are chosen for two fluorophore types, all possible mixed colors (for different V_1 and V_2) are shown using the minor sector of the circle. (b) Demonstration of four-color mixing. The hue, saturation, and value are represented by the azimuthal angle, vertical distance and radial distance respectively. Colors associated with all hue-value combinations are shown at three saturation levels 0, 0.5, and 1. The four colors being mixed have hues of 0° , 90° , 200° and 300° , and values of 0.8, 0.6, 0.4 and 0.3 respectively, which are shown using solid-white arrows. The hue and value of the mixed color are calculated using eqn (3) and (4) based on the sum of the four complex numbers $V_j e^{iH_j}$. The resultant complex number $V_{mix} e^{iH_{mix}}$ is shown by the dashed-white arrow in the $S = 1$ plane. The mixed color has a value of 0.8 and hue of 19.5° . The saturation of mixed color is 0.5 (eqn (5)). The drop in saturation to the $S = 0.5$ plane is shown by the dashed-black arrow.

Existing color mixing techniques often use the RGB (red-green-blue) or CMY (yellow-cyan-magenta) color space. At most three fluorophore types can be superimposed in these methods and they can only be associated with the primary (in RGB) or secondary colors (in CMY). In the HSL (hue-saturation-luminance) color mixing scheme developed by Demanols and Davoust,⁵⁹ I for one fluorophore type can be associated with any fully saturated hue. However, this method cannot mix more than two hues because it does not follow the associative law; consequently, mixing more than two colors is order-dependent. In contrast, the new color mixing scheme presented here is superior to previous methods because an arbitrary number of fully saturated hues can be mixed. This allows great flexibility in choosing hues for different fluorophores, such as choosing color-safe colocalization hues for color-blind readers (SI Section S6). Choice of non-standard colors has the added benefit of producing stronger color contrast in *in-silico* (**Figure 5**) and experimental (SI Section S7) images. Even if the resultant V_{mix} is the same for different color combinations, the contrast in images can be different because the relative luminance⁶⁰ (brightness) is not the same for all hues. For example, relative luminance⁶⁰ is highest for yellow and lowest for blue, with

yellow having ~ 10 times the relative luminance⁶⁰ of blue at the saturation of 1. For further discussion on color contrast and relative luminance,⁶⁰ see SI Section S8.

Time-averaged *in-silico* microscopy images can be generated by superimposing time-averaged *in-silico* monochrome images. The time over which average is performed represents an effective exposure time (**Figure 3e**, and SI Section S9). As fluorophore particles move, a time-averaged image captures the motion blur arising from the particle's motion. When the particle's diffusion coefficient is high so is the motion blur and vice versa. Finally, multiple images generated at different simulation times, with or without time averaging, can be combined to create an *in-silico* microscopy video (**Figure 1e**). The *in-silico* microscopy video associated with **Figure 3e** is provided in SI Video 1-3.

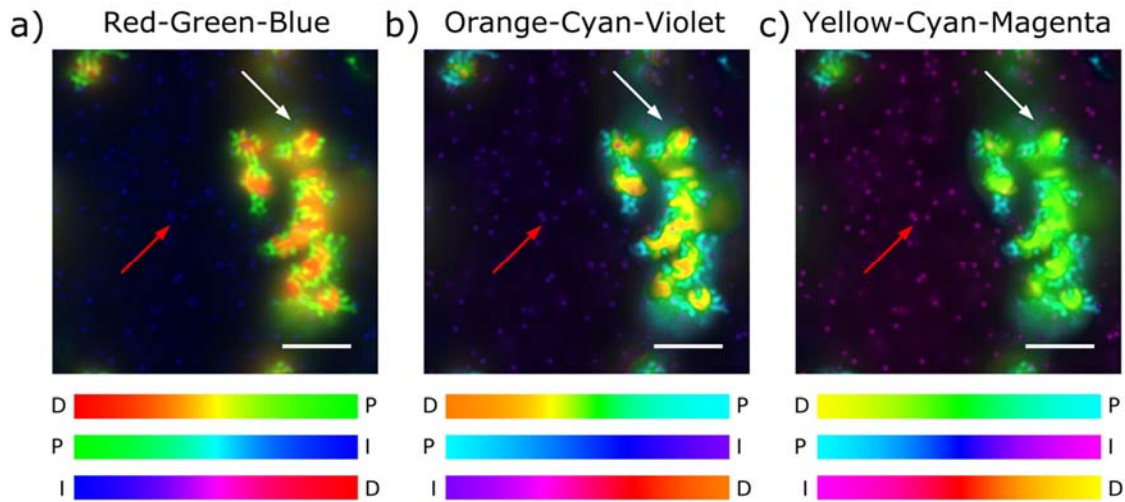


Figure 5. Images with different color combinations. (a) red-green-blue, (b) orange-cyan-violet, and (c) yellow-cyan-magenta (colocalization color bars below each subfigure; D: DNA, P: PEI, I: ions). MS on PEI-DNA aggregation³⁶ (see Methods) at $t = 3 \mu\text{s}$ is used as the virtual specimen where all the PEI and DNA particles, and ions are assumed to emit fluorescence. PSF is modeled with $\beta = 59.4^\circ$, $\mu = 1.51$, n is x -axis, $n_o = 4 \text{ nm}$, $\Delta l' = \Delta m' = 0.1 \text{ nm}$, $\Delta n' = 0.05 \text{ nm}$, $P_l = P_m = P_n = 25 \text{ nm}$, $f_s = 530$, $(\lambda, I_0) = (670 \text{ nm}, 0.13)$ for DNA, $(518 \text{ nm}, 0.27)$ for PEI and $(461 \text{ nm}, 0.4)$ for ions. Visibility for ions over black (red arrow) and non-black (white arrow) backgrounds is dependent on the color combinations. Ion visibility for color combination of D-P-I follows yellow-cyan-magenta > orange-cyan-violet > red-green-blue over black background, and orange-cyan-violet > yellow-cyan-magenta > red-green-blue over non-black background. Overall orange-cyan-violet combination performs best among the three.

Applications. *In-silico* microscopy is operated on MS data using physics-based PSF.

Therefore, similar to experimental images, *in-silico* images should be treated as data⁶¹ of the

underlying MS, and both qualitative and quantitative analyses can be performed on the *in-silico* images. More importantly, since MS has predictive power, MS data associated with *in-silico* images serve as the ground truth, enabling cross-validation, attainment of new knowledge, examination of existing analysis tools, and creation of new analysis tools, to name a few. The wide and versatile application of the *in-silico* microscopy is demonstrated using the following three examples.

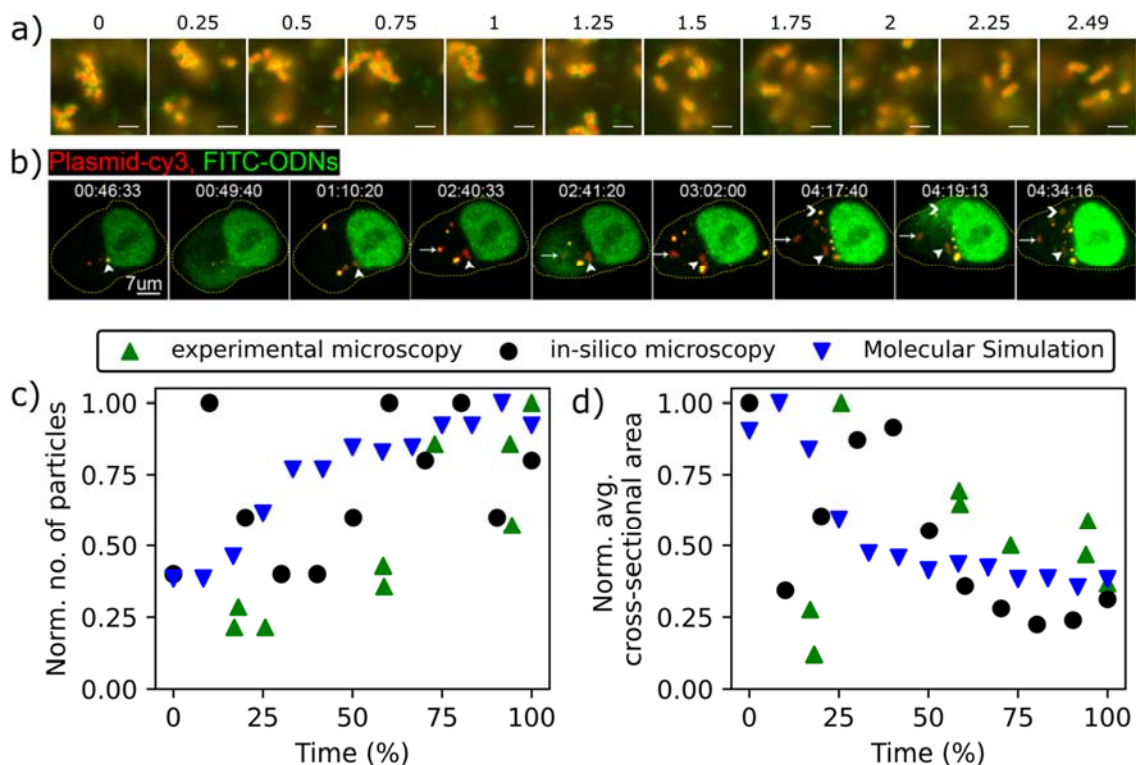


Figure 6. Gaining new information by comparing *in-silico* images, experimental images, and detailed MS data. (a) *In-silico* microscopy images from endosomal acidification simulation of PEI-DNA nanoparticles (see Methods), where PEI and DNA particles are assumed to emit fluorescence. PSF is modeled with $\beta = 59.4^\circ$, $\mu = 1.51$, n is z -axis, $n_O = 0$ nm, $\Delta l' = \Delta m' = 0.1$ nm, $\Delta n' = 0.05$ nm, $P_{l'} = P_{m'} = P_{n'} = 25$ nm, $f_s = 260$, $(\lambda, I_0) = (670$ nm, 0.04) for DNA and (518 nm, 0.06) for PEI; DNA and PEI particles are assigned red and green hues respectively. Above each image, the simulation time is specified in microseconds, with endosomal acidification marking the start of the simulation. Scale bar, 5 nm. (b) Experimental fluorescence microscopy images by Rehman *et al.*² of PEI-mediate delivery of plasmid DNA (red) and oligonucleotides (green). The time is in hours:minutes:second format and the scale bar represents 7 μm . [Reprinted with permission from Rehman *et al.*² Copyright © 2013 American Chemical Society]. (c) The number of particles and (d) cross-sectional area of nanoparticles, normalized by the corresponding maximum value from *in-silico* images, experimental images, and MS data. Threshold of 0.588 and 0.196 was used for *in-silico* and experimental images respectively to calculate the number and cross-sectional area. The cross-sectional area corresponding to MS was calculated from the square of the hydrodynamic radius (see Methods).

First, new information can be gained by comparing data from MS, *in-silico* images, and experimental images. In **Figure 6a**, *in-silico* microscopy images are generated for an endosomal acidification simulation on polyethylenimine (PEI)-DNA nanoparticles (see Methods). In **Figure 6b**, PEI-based delivery of plasmid DNA (red) and oligonucleotides (green) inside HeLa cells is shown, which also undergoes endosomal acidification.² Qualitative similarities between **Figure 6a** and **Figure 6b** (appearance of smaller nanoparticles as time increases) can be established by visual inspection. Quantitatively, the normalized number of particles (**Figure 6c**) and normalized average cross-sectional area of nanoparticles (**Figure 6d**) are calculated (See Methods). In **Figure 6c**, a general increasing trend is observed for both experimental microscopy and MS. The trend from *in-silico* microscopy is less clear due to the large fluctuations caused by particles moving in and out of the focal plane of interest. Similar fluctuation is also observed in experimental microscopy at ~90% of the total time. In **Figure 6d**, a general decreasing trend of average cross-sectional area is observed for *in-silico* microscopy, experimental microscopy, and MS. A transient increase at a short time (10-40% of the total time) is also observed for *in-silico* and experimental microscopy images. Clearly, qualitative and quantitative agreement between MS and experimental microscopy is achieved. In addition, detailed MS data has provided direct evidence for nanoparticle dissociation under endosomal acidification, which means dissociation of plasmid DNA from the nanoparticles likely occurred in Rehman *et al.*² although it was not reported in the original article. The comparison also suggests that an overall decrease in average cross-sectional area is a good indicator for nanoparticle dissociation, which can be used as a new analysis tool for experimental microscopy.

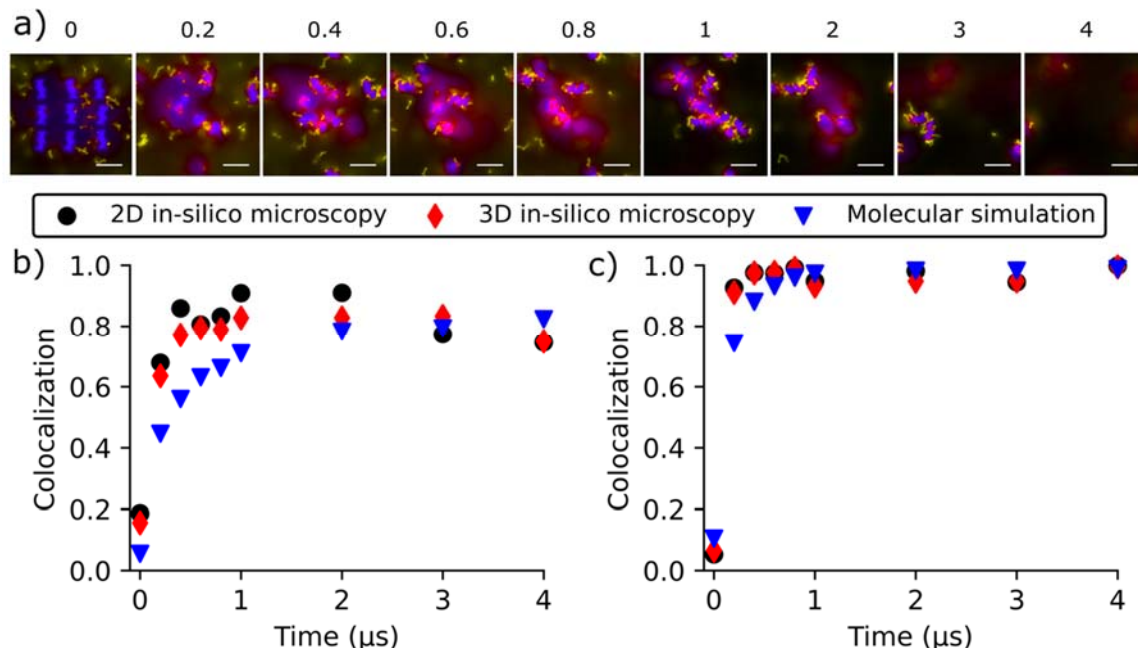


Figure 7. Bridging data obtained from MS and *in-silico* images. (a) *In-silico* microscopy images of PEI-DNA aggregation simulation³⁶ (see Methods) at different times, where PEI and DNA particles are assumed to emit fluorescence, for visual colocalization analysis. The PSF is modeled with $\beta = 59.4^\circ$, $\mu = 1.51$, n is z -axis, $\Delta l' = \Delta m' = 0.1$ nm, $\Delta n' = 0.05$ nm, $P_l = P_m = P_n = 25$ nm, $f_s = 530$, $(\lambda, l_0) = (670$ nm, 0.13) for DNA and (518 nm, 0.27) for PEI; DNA and PEI particles are assigned indigo and yellow hues respectively. 2D images (shown) were generated using $n_O = 12$ nm, and 3D images (not shown) were generated with $\Delta n_O = 1$ nm. The time, in microseconds, is shown above each *in-silico* image. Scale bar, 5 nm. Colocalization analysis was performed using Manders' coefficients¹³ with JACoP plugin⁶² in Fiji ImageJ⁶³: (b) fraction of PEI colocalized with DNA (eqn (6)), and (c) fraction of DNA colocalized with PEI (eqn (7)) were calculated using a threshold of 0.2685 for both PEI and DNA. The MS values in (b) and (c) correspond to the fraction of PEI beads having at least one DNA bead within 0.81 nm, and the fraction of DNA beads having at least one PEI bead within 0.85 nm.

Second, *in-silico* microscopy can bridge the analyses of data from MS and experimental microscopy, despite their distinct data acquisition techniques. **Figure 7a** shows the *in-silico* microscopy images of a PEI-DNA aggregation simulation at different times. The DNAs and PEIs begin unaggregated at 0 μ s and aggregate over time. Complexation of DNA and PEI can be observed as the color of DNAs and PEIs change from indigo and yellow to magenta. Most of the DNAs are complexed at 0.2 μ s. Meanwhile, free PEIs not complexed with DNAs are observed to decrease. The lowest number of free PEI is observed at 1 μ s, whereafter it does not change significantly. Quantitative data can be obtained using a dedicated colocalization analysis, such as Manders' coefficients¹³ M_1 (**Figure 7b**) and M_2 (**Figure 7c**) given by eqn (6) and (7) respectively.

I_{PEI} and I_{DNA} are monochrome intensities of PEI and DNA respectively at a given pixel, I_{thres} is a threshold intensity, $\mathbb{H}(\cdot)$ is the Heaviside step function, and summations are performed over all pixels.⁶² Physically, M_1 is the fraction of total PEI fluorescence that is colocalized with DNAs having fluorescence above the threshold I_{thres} . Similarly, M_2 is the fraction of total DNA fluorescence that is colocalized with PEIs having fluorescence above the threshold I_{thres} . The Manders' coefficients¹³ are calculated from a single 2D image, as well as from multiple 2D images generated using $\Delta n_O = 1$ nm (i.e., 3D *in-silico* microscopy in **Figure 7b-c**).

$$M_1 = \frac{\sum I_{PEI} \mathbb{H}(I_{DNA} - I_{thres})}{\sum I_{PEI}} \quad (6)$$

$$M_2 = \frac{\sum I_{DNA} \mathbb{H}(I_{PEI} - I_{thres})}{\sum I_{DNA}} \quad (7)$$

Using detailed MS data, the fraction of PEI beads that have at least one DNA bead within 0.81 nm shows excellent agreement with M_1 (**Figure 7b**). The cutoff 0.81 nm is the sum between the first minimum in the PSF of PEI and the distance at which the PSF of DNA is equal to the threshold I_{thres} for $n' = 0$. Similarly, the fraction of DNA beads that have at least one PEI bead within 0.85 nm is equivalent to M_2 (**Figure 7c**), where 0.85 nm is the sum between the first minimum in the DNA PSF and the distance at which the PEI PSF is equal to the threshold I_{thres} for $n' = 0$ (see Methods). **Figure 7b-c** shows that the equivalency of properties calculated from MS and *in-silico*, and hence experimental, microscopy images which suggest a way to bridge data analyses in these two completely different fields. The example here also demonstrates that it is feasible to estimate 3D contacts of molecules (and likely other properties) by visual inspection and quantitative analysis of 2D microscopy images (**Figure 7a**).

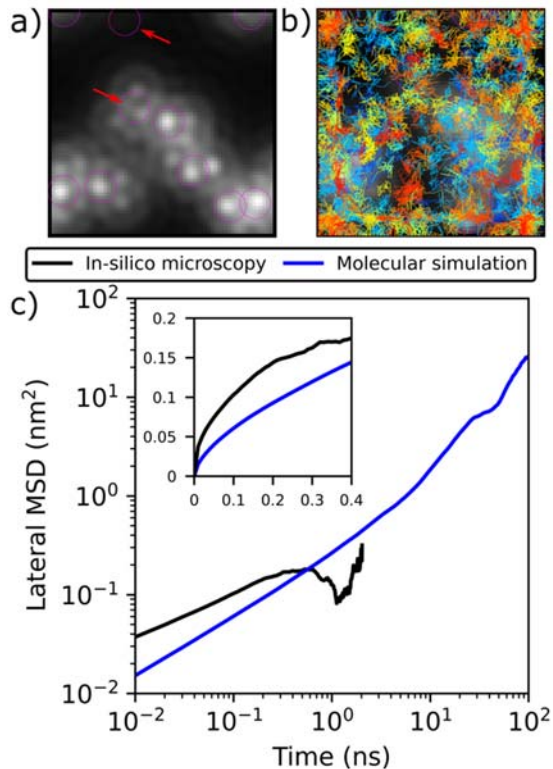


Figure 8. Single-particle tracking using *in-silico* microscopy on MS of dimyristoyl phosphatidylcholine (DMPC) lipid bilayer⁶⁴ (see Methods), where a phosphorous atom in DMPC is assumed to emit fluorescence. (a) *In-silico* microscopy image at time 0 μ s. The PSF is modeled with $\beta = 59.4^\circ$, $\mu = 1.51$, n is z -axis, $n_o = 3$ nm, $\Delta l' = \Delta m' = 0.1$ nm, $\Delta n' = 0.2$ nm, $P_l = P_{m'} = 25$ nm, $P_{n'} = 2$ nm, $f_s = 530$, $(\lambda, I_0) = (670$ nm, 0.7) was used for phosphorous atoms in DMPC. Particles detected by TrackMate⁶⁵ plugin in Fiji ImageJ⁶³ are shown with purple circles. (b) Particle's tracks recognized by TrackMate.⁶⁵ A unique color is assigned to each track. (c) The lateral (in the lm plane) positions of phosphorous atoms as functions of time detected by TrackMate⁶⁵ were used to calculate the lateral mean squared displacement (MSD) and compared with the corresponding value from MS.

Third, *in-silico* microscopy can be used as a platform to assess image analysis tools. In **Figure 8**, single-particle tracking is performed on *in-silico* images of a dimyristoyl phosphatidylcholine (DMPC) lipid bilayer MS⁶⁴ using TrackMate⁶⁵ in Fiji ImageJ⁶³ (see Methods). The phosphorous atom in each DMPC molecule was selected to emit fluorescence (**Figure 8a**). TrackMate⁶⁵ detects several “tracks” of particles (“spots”), which are shown with different colors in **Figure 8b**. As the particles move across the periodic boundary in the MS, they are considered to be different by TrackMate⁶⁵ and therefore produce new “tracks”. The lateral mean-squared-displacement (MSD) calculated from “tracks” with more than 20 consecutive particle positions is shown in **Figure 8c** (see Methods). Due to PBC, the “tracks” are short and the sampling is poor

beyond 1 ns. Such sampling issues are not observed when lateral MSD is calculated directly from MS (with *msd* function in Gromacs) using positions of only phosphorous atoms and PBC (**Figure 8c**). The lateral MSD determined from MS and *in-silico* images are significantly different even at a short time (< 0.4 ns). This difference is not caused by PBC because the sampling is sufficient within such a short time; rather it is likely due to incorrect detection of particles (for example arrows in **Figure 8a**) and “tracks”. The lateral diffusion coefficient can be calculated by dividing the slope of the lateral MSD vs. time plot in linear scale by a factor of 4. The results from MS and *in-silico* images are respectively 6.17×10^{-7} cm²/s and 51.6×10^{-7} cm²/s, a more than 8-fold difference. Researchers therefore should exercise caution when directly applying particle tracking to experimental microscopy images to evaluate the mobility of the particles. As an alternative approach, we demonstrate that diffusion coefficients can be calculated using FCS on *in-silico* images, which agree better with MS simulation results (SI Section S10).

To demonstrate the applications of the *in-silico* microscopy, in the examples above non-fluorophore particles are assumed to emit fluorescence. It is recognized that the presence of fluorophores in a real sample may affect the dynamics and even interact with the molecules of interest (e.g., PEIs and DNAs). Such effect can be addressed by explicitly including the fluorophores in the MS, as well as by modeling accurate photophysics of fluorophores (SI Section S4). In fact, the *in-silico* microscopy can provide a means to test the accuracy of modeling the photophysical processes and interactions of fluorophores, by generating *in-silico* images with different models and comparing them with experimental images.

Discussions

A novel *in-silico* fluorescence microscopy is presented as an open-source toolbox (in-silico-microscopy, v1.2.2), which can work with different optical axis, object focal plane, exposure time,

and color combinations; and generate images and videos with the desired resolution, contrast, brightness, and amount out-of-focus fluorescence. The toolbox has the capability of capturing photophysical processes such as photoblinking, photobleaching, phosphorescence, and fluorescence with multiple wavelengths (SI Section S4). Images that resemble experimental widefield, OSM, and super-resolution microscopy images can be generated by changing parameters such as the amount of out-of-focus fluorescence and FWHM scaling factor (see SI Section S2 for more details). Properties calculated from different experimental microscopies will differ and corresponding *in-silico* microscopies can be used to quantify the difference. Other fluorescence microscopies can also be modeled by changing the PSF,^{46,66,67} which is allowed by the modular nature of the toolbox. Moreover, PSF obtained from experiments can be implemented to model non-ideal objective lens with aberration.²⁸ It is recognized that some fluorescence microscopies such as structure illuminated microscopy^{68,69} (SIM), Förster resonance energy transfer^{70,71} (FRET) microscopy, *etc.* involve mechanisms other than diffraction of light and cannot be modeled by simply changing the PSF. Nevertheless, our powerful toolbox has laid the foundation to generate *in-silico* fluorescence microscopy images that can be compared to those and other techniques such as X-ray microscopy (can be modeled with a PSF⁷²), which would greatly enhance cross-validation and integration between simulations and experiments.

Generally, any image analysis developed for experimental microscopy is also applicable to *in-silico* microscopy, making the list of applications long. Three major categories of applications are presented in this work, namely generating new information by cross-comparison, determining equivalence of properties calculated from MS and experiments, and assessing image analysis tools or estimating errors using MS-based ground truth. For the former two, similar experimental and MS systems are required, which is possible in many fields of research such as gene delivery (shown in Results), biological motors,⁷³ role of lipid in membrane organization,⁷⁴ chromosomal

dynamics,⁷⁵ *etc.* Error estimation for imaging analysis is a common practice in the literature where randomly placed objects are usually used as the ground truth.^{47–50} The *in-silico* microscopy enables the use of MS data as the ground truth, which is physics-based, dynamic, and more realistic than synthetic data. For better comparison with experiments, *in-silico* images can be generated with and without noise (SI Section S11), before and after deconvolution (SI Section S12), further demonstrating the versatility of the toolbox. Care should be taken while using existing image analysis tools, as these algorithms do not employ PBC which may be present in some MS. The existence of PBC in the MS does not affect analysis such as colocalization, fluorescence intensity, FCS and fluorescence cross-correlation spectroscopy (FCCS) (SI Section S10), or deconvolution (SI Section S12), while it might affect the calculation of count, radius, area, volume, and shape if the fluorescence of the particles is divided across the periodic boundary (**Figure 9**). In the toolbox v1.2.2 provided, count, area, and volume can be evaluated with the presence of PBC, while existing image analysis algorithms do not yet have this capability.

Compared to existing studies in the literature,^{51,52,54,55} this work has detailed considerations of the PSF, color, and applications. Moreover, our toolbox can model phosphorescence and a fluorophore emitting fluorescence of multiple wavelengths (to simulate emission spectra), which has not been achieved before. The work by Angiolini *et al.*,⁵² Watabe *et al.*,⁵⁴ and Lindén *et al.*⁵⁵ uses reaction-diffusion models, which cannot capture molecular interactions and thereby do not have the predictive power of MS. Dix *et al.*⁵¹ performed a MS but only considered simple particles without elaborate intermolecular interaction. Furthermore, their application was limited to FCS analysis over a control volume and did not produce spatial fluorescence data such as *in-silico* images or videos. In contrast, our work can model FCS and FCCS, as well as generate *in-silico* microscopy images and videos which has additional applications as demonstrated above. The work by Girsault *et al.*⁴⁹ is also worth mentioning, which modeled super-resolution optical imaging

(SOFI) and stochastic optical reconstruction microscopy (STORM) for randomly placed fluorophores. These microscopy techniques use multiple diffraction-limited images and improve their resolution based on photoblinking (STORM) or fluctuations in fluorescence intensity (SOFI). Our toolbox can be integrated with these techniques to perform *in-silico* SOFI and STORM.

Software such as visual molecular dynamics (VMD) can visualize 3D structures, where the particles' colors are linearly blended with the background color according to the depth of the particles. As a result, it is difficult to visually estimate distances between particles. Furthermore, the opacity of the particles limits the view of the particles behind, and increasing transparency worsens the depth perception. Typically, the proximity of particles at a specific time is determined by rotating/translating the MS system and zooming into the area of interest, which is a time-consuming process. The toolbox presented here can be used as a standalone visualization tool for MS, where complex 3D data is condensed into 2D images. Key features from the plane of interest (object focal plane) are stored in high resolution, while the information away from the plane of interest is stored in low resolution. The proximity between two or more types of particles can be visualized using their colocalized hues, which is superior to depth perception in software like VMD. For example, in **Figure 7** it is demonstrated that 3D contacts can be predicted with a visual inspection of 2D images. Other plausible applications include the analysis of morphological changes in molecules, aggregation or dissociation of molecules, multi-phase diffusion, *etc.* While *in-silico* images are corrupted by PSF, the amount of corruption can be controlled using the FWHM scaling factor or by changing the functional form of PSF, which does not need to model a microscope when used as a visualization tool. The visualization of colocalized fluorophores is improved using the newly developed color mixing scheme for both *in-silico* (**Figure 5**) and experimental (SI Section S7) images, representing an added strength of the standalone visualization tool.

Although the toolbox is developed for MS such as molecular dynamics, microscopy images can be generated for other non-molecular simulations such as the finite element method (FEM), by treating the nodes in an FEM mesh as particles (the FEM nodes data must be converted to “gro” coordinate file format to be directly usable by the v1.2.2 of the toolbox). For continuum-level models such as Poisson-Boltzmann, where discrete position coordinates are unavailable, the general methodology demonstrated in this work can still be applied to create microscopy images by the convolution of PSF and particle densities in continuous form.

Conclusion

A novel open-source toolbox for performing *in-silico* (virtual) fluorescence microscopy on molecular simulations is presented. The toolbox can generate *in-silico* microscopy images that models different experimental fluorescence microscopies as well as photophysical processes of fluorophores. This brings the seemingly remote fields of microscopy and simulations together by generating new knowledge from direct cross-validation, determining equivalence of properties extracted from MS and experimental images, assessing and developing algorithms for experimental image analysis, *etc.* The ability to form a direct bridge between experimental microscopy and molecular simulation can enhance our understanding on many biomolecular processes such as chemical kinetics, diffusion, binding of lipids, proteins and nucleic acids, gene delivery, and chromosomal dynamics, to name a few. It also paves the path for other *in-silico* microscopy techniques applied to molecular and non-molecular simulations. The work also reports the development of a new color mixing scheme, which allows the visualization of multi-fluorophore colocalization with an arbitrary color assignment to the fluorophores. We expect this to be beneficial for *in-silico* microscopy, experimental fluorescence microscopy, and standalone

visualization tools. We further hope this new open-source toolbox would spread the joy of creating and observing beautiful and powerful images, to theoreticians and experimentalists alike.

Methods

Generating *in-silico* microscopy images and videos. The *in-silico* monochrome images were rendered using *matplotlib*⁷⁶ *imshow* with a grey colormap. A 2D cross-sectional view depicting the use of PBC and a white image frame is shown in **Figure 9**. The number of periodic images of fluorophores that contribute to $I(l', m', n_o, \lambda, t)$ depends on the dimensions (P_l, P_m, P_n) specified for the predetermination of PSF. However, the range of (l', m') coordinates corresponds to the original MS specimen (center box in \mathcal{MS} , **Figure 2**). For example, if an MS specimen is a cube with side length of 100 nm and $P_l, P_m, P_n = 300$ nm, I will be calculated for the image coordinates $0 \leq l', m' \leq 100$ nm, while particles (and their periodic images) located at $l \in [l' - 150, l' + 150]$, $m \in [m' - 150, m' + 150]$ and $n \in [n' - 150, n' + 150]$ can all contribute to I at (l', m') . In each direction l or m , the dimension of the white image frame is greater than or equal to the largest MS specimen during the entire trajectory. For example, if an MS simulation produces two MS specimens with dimensions of (100, 200, 300) and (200, 100, 300) nm in the lmn directions, the white image frame is no smaller than 200×200 nm².

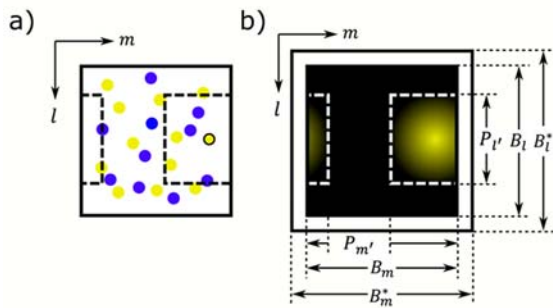


Figure 9. Handling of periodic boundary condition and white frame. a) MS box when seen along the optical axis n . The lm axes are shown for reference. The yellow and indigo circles represent particles of two different fluorophore types. The PSF for the yellow circle with a black outline is calculated over a 3D cuboidal box centered around it with dimension (P_l, P_m, P_n) . The 2D cross-sectional view of the box with dimension (P_l, P_m) is shown by black dashed lines, which is split into two parts due to PBC. b) The image is generated from the fluorescence of the yellow particle with a black outline shown in (a). The largest MS box in the trajectory is represented by the white frame with

dimensions B_l^* and B_m^* . The MS box for the current time is represented by the black background with dimensions B_l and B_m and placed at the center of the white image frame.

For generating colored microscopy images, all mixed HSV colors were converted to RGB colors based on Smith⁷⁷ before rendering each *in-silico* microscopy image. The final *in-silico* microscopy images were produced using *imshow* in *matplotlib*⁷⁶ v3.1.3. Videos were created in .mov format with ‘mp4v’ codec using VideoWriter class from OpenCV-python v.3.4.4 (<https://libraries.io/pypi/opencv-python/3.4.4.19>). The toolbox also allows the generation of microscopy images as TIFF format which can handle multidimensional images.

Molecular simulations. The PEI-DNA aggregation simulation used in this work was a MARTINI coarse-grained molecular dynamics simulation³⁶ performed using the GROMACS 5 package.⁷⁸ The system contained 27 DNAs, 270 PEIs, and 150 mM KCl. In the initial configuration, the DNAs were arranged in a 3x3x3 cubic lattice inside a cubic box of side 25 nm, with 6 nm as the closest distance between the centers of mass of two DNAs. The PEIs and ions were placed randomly in the cubic box. The configuration of the system after energy minimization using steepest-descent and constrained simulation of 1 ns in NPT ensemble is shown in **Figure 1b**. Thereafter, an unconstrained NPT simulation was run for 4 μ s. In the constrained NPT simulation, all bonds in PEI and water, and backbone bonds in DNA were constrained. A cut-off radius of 1.1 nm was chosen for van der Waal’s interactions using the potential-shift-Verlet scheme in GROMACS. Electrostatic interactions were modeled using short-range Coulombic interactions with a relative dielectric constant of 2.5 and cut-off radius of 1.1 nm, as well as long-range reaction-field⁷⁹ interactions with a relative dielectric constant of ∞ .⁸⁰ A neighbor list with the cut-off radius of 1.1 nm was updated every 20 steps using the Verlet scheme.⁸¹ Berendsen barostat was used with a time constant of 3 ps and compressibility of 3×10^{-4} bar⁻¹ to maintain the pressure at 1 bar. Initial velocities were generated from Maxwell-Boltzmann distribution for the temperature of 300 K. The

temperature was then maintained using a velocity-rescaling thermostat with a time constant of 0.1 ps.⁸² The leap-frog integrator was used with the timestep of 5 fs, and periodic boundary condition was applied in all directions. A time-scaling factor of 4 was used to scale the reported simulation time. Unconstrained NPT simulation was similar to constrained NPT simulation with three differences. First, Parrinello-Rahman barostat was used with a time constant of 5 ps and compressibility of $4.5 \times 10^{-5} \text{ bar}^{-1}$. Second, constraints were only applied to bonds in the water molecules. Third, initial velocities were obtained from the last step of constrained NPT simulation.

The last configuration of the PEI-DNA aggregation simulation was used as the initial configuration for the endosomal acidification simulation. To simulate acidification, every 0.4 ns the protonation ratio of a randomly selected PEI was changed from 23% to 46%, followed by adding an appropriate number of chloride ions to keep the system electroneutral. After all PEIs were acidified (in 108 ns), an unconstrained NPT simulation was run for an additional 2.5 μs . Acidification simulation did not involve constrained NPT simulation, and the settings for the unconstrained simulation were the same as described above.

The DMPC lipid bilayer simulation dataset produced by Miettinen⁶⁴ (Copyright © 2013 Miettinen, Creative Commons Attribution 4.0 International License) was used to calculate mean-squared-displacement. The system consisted of 128 DMPC and 5097 SPC water molecules and was run for 110 ns in an unconstrained NPT ensemble using the Gromacs 3⁸³ package.

Analysis of *in-silico* microscopy images. To determine the number and cross-sectional area of particles from an *in-silico* image, a binary image was produced using a threshold intensity; any pixel with intensity above the threshold was considered to be part of a particle. If two pixels were vertically or horizontally adjacent (while considering PBC) to each other and both have intensity above the threshold, they were considered to be part of the same particle; pixels diagonal to each other were not considered to be adjacent. Pixels belonging to the same particle were grouped. The

number of such groups was defined as the number of particles, and the cross-sectional area of a particle was calculated from the product between the number of pixels in the particle and the area of a pixel ($\Delta l' \Delta m'$). For experimental images, the number of particles and cross-sectional area were calculated using the “Analyze Particles” feature in Fiji ImageJ.⁶³ The number of particles and cross-sectional area were then normalized by their corresponding maximum values.

Single-particle tracking was performed using TrackMate v6.0.2 in Fiji ImageJ.^{63,65} Voxel dimensions were calibrated to the grid used for PSF calculation, i.e., $(\Delta l', \Delta m') = (0.1, 0.1)$ nm. The time interval was set as 1 ns (based on the lipid simulation⁶⁴). The entire image was used for analysis, i.e., crop settings were set to default. Particles were detected using Laplacian of Gaussian detector with an “estimated blob diameter” of 9.0 and threshold diameter of 6.0. All detected particles were selected for tracking using the “Simple LAP” tracker. Maximum linking distance, gap-closing distance, and gap-closing frame gap were set to 5.0, 5.0, and 2 respectively. Lateral MSD was calculated using $MSD(t) = \langle |\mathbf{r}(t + t_0) - \mathbf{r}(t_0)|^2 \rangle$, where \mathbf{r} was the 2D position vector of a particle (l, m) , and the average $\langle \cdot \rangle$ was performed over different “tracks” and different reference time t_0 .

Analysis of MS data. The number of nanoparticles in a MS was calculated based on Mahajan and Tang.³⁶ PEIs and DNAs were considered to be bound if their minimum distance was less than 0.528 nm. A PEI-DNA nanoparticle was a collection of all PEIs and DNAs bound to each other. At each time, the number of nanoparticles was averaged over 10 ns after this time. Hydrodynamic radius of a nanoparticle was calculated using $R_{hyd} = N^2 / \langle \sum_{i < j} 1/r_{ij} \rangle$, where N was the number of beads in a nanoparticle (including those from both PEIs and DNAs), r_{ij} was the distance between beads i and j , and $\langle \cdot \rangle$ represented ensemble average.⁸⁴ Cross-sectional area of nanoparticles was approximated by R_{hyd}^2 averaged over 10 ns.

The fraction of PEI beads that had at least one DNA bead within a cutoff distance was determined using the *mindist* function in Gromacs. The total number of contacts between PEIs and DNAs was calculated using the *group* option where all DNAs were specified as the first group. That is, contacts between a PEI bead and multiple DNA beads were treated as one. Then, the number of contacts was divided by the total number of PEI beads to obtain the fraction of PEI beads in contact with at least one DNA bead. A similar approach was taken to determine the fraction of DNA beads in contact with at least one PEI bead.

Associated Content

Data and Code availability

The data that support the findings of this study are openly available in the University of Alberta Libraries Dataverse network at <https://doi.org/10.7939/DVN/F3JKZH>, Version 2.1. The open-source codes used in this work along with tutorials are maintained on GitHub, <https://github.com/subhamoymahajan/in-silico-microscopy>. This article is based on version v1.2.2.

Acknowledgements

We acknowledge the computing resources and technical support from Western Canada Research Grid (WestGrid).

Funding Sources

T. T. acknowledges financial support from the Natural Sciences and Engineering Research Council of Canada (NSERC; Grant number: RGPIN-2018-04281, RGPAS-2018-522655). S. M. is grateful for the Sadler Graduate Scholarship, Alberta Graduate Excellence Scholarship, R. R. Gilpin Memorial Scholarship, and Mitacs Globalink Graduate Fellowship.

Author contributions

S. M. formulated the idea, developed methods, wrote the software, analyzed, validated, and visualized data, and prepared the original draft of the manuscript. T. T. supervised, acquired financial support, arranged computational resources, checked results, and provided a critical review of the manuscript. S. M. and T. T. equally contributed to formulating the color mixing method.

Notes

The authors declare no competing financial interests.

Supporting Information. The Supporting Information is available free of charge via the internet at <http://pubs.acs.org>. Additional discussions on Point spread function for *in-silico* microscopy; Modes of *in-silico* microscopy; Choosing maximum fluorescence intensity and FWHM scaling factor; Modeling photophysical processes; Development of color mixing scheme; Choosing hues for fluorophore types; Implementing color-mixing scheme on experimental images; Luminance of hues and its effects on color contrast; Time-integrated and time-averaged images; Fluorescence correlation and cross-correlation spectroscopy; Adding Poisson-Gaussian noise; Deconvolution of *in-silico* microscopy images; Supplementary video 1-3 demonstrating PEI-DNA aggregation with different exposure times.

References

- (1) Huang, B.; Bates, M.; Zhuang, X. Super-Resolution Fluorescence Microscopy. *Annu. Rev. Biochem.* **2009**, *78*, 993–1016.
- (2) Rehman, Z. U.; Hoekstra, D.; Zuhorn, I. S. Mechanism of Polyplex- and Lipoplex-Mediated Delivery of Nucleic Acids: Real-Time Visualization of Transient Membrane Destabilization Without Endosomal Lysis. *ACS Nano* **2013**, *7* (5), 3767–3777.
- (3) Frederiksen, R. S.; Alarcon-Llado, E.; Krogstrup, P.; Bojarskaite, L.; Buch-Månson, N.; Bolinsson, J.; Nygård, J.; Morral, A. F. i; Martinez, K. L. Nanowire-Aperture Probe: Local Enhanced Fluorescence Detection for the Investigation of Live Cells at the Nanoscale. *ACS Photonics* **2016**, *3* (7), 1208–1216.
- (4) Erickson, H. P. Size and Shape of Protein Molecules at the Nanometer Level Determined by Sedimentation, Gel Filtration, and Electron Microscopy. *Biol. Proc. Online* **2009**, *11* (1), 32–51.
- (5) Jeynes, J. C. G.; Geraki, K.; Jeynes, C.; Zhaohong, M.; Bettioli, A. A.; Latorre, E.; Harries,

- L. W.; Soeller, C. Nanoscale Properties of Human Telomeres Measured with a Dual Purpose X-Ray Fluorescence and Super Resolution Microscopy Gold Nanoparticle Probe. *ACS Nano* **2017**, *11* (12), 12632–12640.
- (6) Ahmadi, Y.; Nord, A. L.; Wilson, A. J.; Hütter, C.; Schroeder, F.; Beeby, M.; Barišić, I. The Brownian and Flow-Driven Rotational Dynamics of a Multicomponent DNA Origami-Based Rotor. *Small* **2020**, *16* (22), 2001855.
 - (7) Melitz, W.; Shen, J.; Kummel, A. C.; Lee, S. Kelvin Probe Force Microscopy and Its Application. *Surf. Sci. Rep.* **2011**, *66* (1), 1–27.
 - (8) Giessibl, F. J. Advances in Atomic Force Microscopy. *Rev. Modern Phys.* **2003**, *75* (3), 949–983.
 - (9) Huang, B.; Babcock, H.; Zhuang, X. Breaking the Diffraction Barrier: Super-Resolution Imaging of Cells. *Cell* **2010**, *143* (7), 1047–1058.
 - (10) Taylor, D. L.; Wang, Y.-L. Fluorescently Labelled Molecules as Probes of the Structure and Function of Living Cells. *Nature* **1980**, *284*, 405–410.
 - (11) Valm, A. M.; Cohen, S.; Legant, W. R.; Melunis, J.; Hershberg, U.; Wait, E.; Cohen, A. R.; Davidson, M. W.; Betzig, E.; Lippincott-Schwartz, J. Applying Systems-Level Spectral Imaging and Analysis to Reveal the Organelle Interactome. *Nature* **2017**, *546*, 162–167.
 - (12) Adhikari, S.; Moscatelli, J.; Smith, E. M.; Banerjee, C.; Puchner, E. M. Single-Molecule Localization Microscopy and Tracking With Red-Shifted States of Conventional BODIPY Conjugates in Living Cells. *Nat. Commun.* **2019**, *10*, 3400.
 - (13) Manders, E. M. M.; Verbeek, F. J.; Aten, J. A. Measurement of Co-Localization of Objects in Dual-Color Confocal Images. *J. Microsc.* **1993**, *169* (3), 375–382.
 - (14) Qamar, S.; Wang, G.; Randle, S. J.; Ruggeri, F. S.; Varela, J. A.; Lin, J. Q.; Phillips, E. C.; Miyashita, A.; Williams, D.; Ströhl, F.; et al. FUS Phase Separation Is Modulated by a Molecular Chaperone and Methylation of Arginine Cation- π Interactions. *Cell* **2018**, *173* (3), 720–734.
 - (15) Capoulade, J.; Wachsmuth, M.; Hufnagel, L.; Knop, M. Quantitative Fluorescence Imaging of Protein Diffusion and Interaction in Living Cells. *Nat. Biotechnol.* **2011**, *29* (9), 835–839.
 - (16) Chong, S.; Dugast-Darzacq, C.; Liu, Z.; Dong, P.; Dailey, G. M.; Cattoglio, C.; Heckert, A.; Banala, S.; Lavis, L.; Darzacq, X.; et al. Imaging Dynamic and Selective Low-Complexity Domain Interactions That Control Gene Transcription. *Science* **2018**, *361* (6400), eaar2555.
 - (17) Mauthe, M.; Orhon, I.; Rocchi, C.; Zhou, X.; Luhr, M.; Hijlkema, K.-J.; Coppes, R. P.; Engedal, N.; Mari, M.; Reggiori, F. Chloroquine Inhibits Autophagic Flux by Decreasing Autophagosome-Lysosome Fusion. *Autophagy* **2018**, *14* (8), 1435–1455.
 - (18) Xu, Z.; Song, W.; Crozier, K. B. Direct Particle Tracking Observation and Brownian Dynamics Simulations of a Single Nanoparticle Optically Trapped by a Plasmonic Nanoaperture. *ACS Photonics* **2018**, *5*, 2850–2859.
 - (19) Schermelleh, L.; Ferrand, A.; Huser, T.; Eggeling, C.; Sauer, M.; Biehlmaier, O.; Drummen, G. P. C. Super-Resolution Microscopy Demystified. *Nat. Cell Biol.* **2019**, *21*, 72–84.
 - (20) Sahl, S. J.; Hell, S. W.; Jakobs, S. Fluorescence Nanoscopy in Cell Biology. *Nat. Rev. Mol. Cell Biol.* **2017**, *18*, 685–701.
 - (21) Lichtman, J. W.; Conchello, J. Fluorescence Microscopy. *Nat. Methods* **2005**, *2* (12), 910–919.
 - (22) Stephens, D. J.; Allan, V. J. Light Microscopy Techniques for Live Cell Imaging. *Science* **2003**, *300* (5616), 82–86.
 - (23) Abbe, E. Beiträge Zur Theorie Des Mikroskops Und Der Mikroskopischen Wahrnehmung. *Arch. für mikroskopische Anat.* **1873**, *9*, 413–468.

- (24) Webb, R. H. Confocal Optical Microscopy. *Reports Prog. Phys.* **1996**, *59* (3), 427–471.
- (25) Huysken, J.; Swoger, J.; del Bene, F.; Wittbrodt, J.; Stelzer, E. H. K. Optical Sectioning Deep Inside Live Embryos by Selective Plane Illumination Microscopy. *Science* **2004**, *305* (5686), 1007–1009.
- (26) Denk, W.; Strickler, J. H.; Webb, W. W. Two-Photon Laser Scanning Fluorescence Microscopy. *Science* **1990**, *248* (4951), 73–76.
- (27) Preza, C.; Ollinger, J. M.; McNally, J. G.; Thomas Jr, L. J. Point-Spread Sensitivity Analysis for Computational Optical-Sectioning Microscopy. *Micron Microsc. Acta* **1992**, *23* (4), 501–513.
- (28) McNally, J. G.; Preza, C.; Conchello, J.-A.; Thomas, L. J. Artifacts in Computational Optical-Sectioning Microscopy. *J. Opt. Soc. Am. A* **1994**, *11* (3), 1056–1067.
- (29) Sarder, P.; Nehorai, A. Deconvolution Methods for 3-D Fluorescence Microscopy Images. *IEEE Signal Process. Mag.* **2006**, *23*, 32–45.
- (30) Gustafsson, M. G. L. Surpassing the Lateral Resolution Limit by a Factor of Two Using Structured Illumination Microscopy. *J. Microsc.* **2000**, *198* (2), 82–87.
- (31) Hell, S. W.; Wichmann, J. Breaking the Diffraction Resolution Limit by Stimulated Emission: Stimulated-Emission-Depletion Fluorescence Microscopy. *Opt. Lett.* **1994**, *19* (11), 780–782.
- (32) Rust, M. J.; Bates, M.; Zhuang, X. Sub-Diffraction-Limit Imaging by Stochastic Optical Reconstruction Microscopy (STORM). *Nat. Methods* **2006**, *3* (10), 793–796.
- (33) Xu, J.; Tehrani, K. F.; Kner, P. Multicolor 3D Super-Resolution Imaging by Quantum Dot Stochastic Optical Reconstruction Microscopy. *ACS Nano* **2015**, *9* (3), 2917–2925.
- (34) Liu, W.; Toussaint Jr., K. C.; Okoro, C.; Zhu, D.; Chen, Y.; Kuang, C.; Liu, X. Breaking the Axial Diffraction Limit: A Guide to Axial Super-Resolution Fluorescence Microscopy. *Laser Photon. Rev.* **2018**, *12* (8), 1700333.
- (35) Yuan, H.; Huang, C.; Li, J.; Lykotrafitis, G.; Zhang, S. One-Particle-Thick, Solvent-Free, Coarse-Grained Model for Biological and Biomimetic Fluid Membranes. *Phys. Rev. E* **2010**, *82*, 011905.
- (36) Mahajan, S.; Tang, T. Polyethylenimine-DNA Ratio Strongly Affects Their Nanoparticle Formation: A Large-Scale Coarse-Grained Molecular Dynamics Study. *J. Phys. Chem. B* **2019**, *123* (45), 9629–9640.
- (37) Uusitalo, J. J.; Ingólfsson, H. I.; Akhshi, P.; Tieleman, D. P.; Marrink, S. J. Martini Coarse-Grained Force Field: Extension to DNA. *J. Chem. Theory Comput.* **2015**, *11* (8), 3932–3945.
- (38) Jung, J.; Nishima, W.; Daniels, M.; Bascom, G.; Kobayashi, C.; Adedoyin, A.; Wall, M.; Lappala, A.; Phillips, D.; Fischer, W.; et al. Scaling Molecular Dynamics beyond 100,000 Processor Cores for Large-Scale Biophysical Simulations. *J. Comput. Chem.* **2019**, *40* (21), 1919–1930.
- (39) Ingólfsson, H. I.; Arnarez, C.; Periolo, X.; Marrink, S. J. Computational ‘Microscopy’ of Cellular Membranes. *J. Cell Sci.* **2016**, *129* (2), 257–268.
- (40) Dror, R. O.; Dirks, R. M.; Grossman, J. P.; Xu, H.; Shaw, D. E. Biomolecular Simulation: A Computational Microscope for Molecular Biology. *Annu. Rev. Biophys.* **2012**, *41* (1), 429–452.
- (41) Navruz, I.; Coskun, A. F.; Wong, J.; Mohammad, S.; Tseng, D.; Nagi, R.; Phillipsac, S.; Ozcan, A. Smart-Phone Based Computational Microscopy Using Multi-Frame Contact Imaging on a Fiber-Optic Array. *Lab Chip* **2013**, *13* (20), 4015–4023.
- (42) Aidukas, T.; Eckert, R.; Harvey, A. R.; Waller, L.; Konda, P. C. Low-Cost, Sub-Micron Resolution, Wide-Field Computational Microscopy Using Opensource Hardware. *Sci. Rep.*

- 2019**, *9* (1), 7457.
- (43) Gibson, S. F.; Lanni, F. Experimental Test of an Analytical Model of Aberration in an Oil-Immersion Objective Lens Used in Three-Dimensional Light Microscopy. *J. Opt. Soc. Am. A* **1992**, *9*, 154–166.
 - (44) Gandy, R. O. Out-of-Focus Diffraction Patterns for Microscope Objectives. *Proc. Phys. Soc. B* **1954**, *67*, 825–831.
 - (45) Richards, B.; Wolf, E. Electromagnetic Diffraction in Optical Systems, II. Structure of the Image Field in an Aplanatic System. *Proc. R. Soc. London A* **1959**, *253* (1274), 358–379.
 - (46) Hell, S.; Reiner, G.; Cremer, C.; Stelzer, E. H. K. Aberrations in Confocal Fluorescence Microscopy Induced by Mismatches in Refractive Index. *J. Microsc.* **1993**, *169* (3), 391–405.
 - (47) Sehayek, S.; Gidi, Y.; Glembockyte, V.; Brandaõ, H. B.; François, P.; Cosa, G.; Wiseman, P. W. A High-Throughput Image Correlation Method for Rapid Analysis of Fluorophore Photoblinking and Photobleaching Rates. *ACS Nano* **2019**, *13* (10), 11955–11966.
 - (48) Lehmußola, A.; Ruusuvoori, P.; Selinummi, J.; Huttunen, H.; Yli-Harja, O. Computational Framework for Simulating Fluorescence Microscope Images With Cell Populations. *IEEE Trans. Med. Imaging* **2007**, *26* (7), 1010–1016.
 - (49) Girsault, A.; Lukes, T.; Sharipov, A.; Geissbuehler, S.; Leutenegger, M.; Vandenberg, W.; Dedecker, P.; Hofkens, J.; Lasser, T. SOFI Simulation Tool: A Software Package for Simulating and Testing Super-Resolution Optical Fluctuation Imaging. *PLoS One* **2016**, *11* (9), e0161602.
 - (50) Venkataramani, V.; Herrmannsdörfer, F.; Heilemann, M.; Kuner, T. SuReSim: Simulating Localization Microscopy Experiments From Ground Truth Models. *Nat. Methods* **2016**, *13* (4), 319–321.
 - (51) Dix, J. A.; Hom, E. F. Y.; Verkman, A. S. Fluorescence Correlation Spectroscopy Simulations of Photophysical Phenomena and Molecular Interactions: A Molecular Dynamics/Monte Carlo Approach. *J. Phys. Chem. B* **2006**, *110* (4), 1896–1906.
 - (52) Angiolini, J.; Plachta, N.; Mocskos, E.; Levi, V. Exploring the Dynamics of Cell Processes through Simulations of Fluorescence Microscopy Experiments. *Biophys. J.* **2015**, *108* (11), 2613–2618.
 - (53) Macháň, R.; Wohland, T. Recent Applications of Fluorescence Correlation Spectroscopy in Live Systems. *FEBS Lett.* **2014**, *588*, 3571–3584.
 - (54) Watabe, M.; Arjunan, S. N. V.; Fukushima, S.; Iwamoto, K.; Kozuka, J.; Matsuoka, S.; Shindo, Y.; Ueda, M.; Takahashi, K. A Computational Framework for Bioimaging Simulation. *PLoS One* **2015**, *10* (7), e0130089.
 - (55) Lindén, M.; Ćurić, V.; Boucharin, A.; Fange, D.; Elf, J. Simulated Single Molecule Microscopy with SMeagol. *Bioinformatics* **2016**, *32* (15), 2394–2395.
 - (56) Webb, D. J.; Brown, C. M. Epi-Fluorescence Microscopy. In *Cell Imaging Techniques. Methods in Molecular Biology (Methods and Protocols)*, vol 931.; Humana Press, Totowa, NJ, 2012; pp 29–60.
 - (57) Xia, J.; Kim, S. H. H.; Macmillan, S.; Truant, R. Practical Three Color Live Cell Imaging by Widefield Microscopy. *Biol. Proc. Online* **2006**, *8* (1), 63–68.
 - (58) Hell, S. W. Toward Fluorescence Nanoscopy. *Nat. Biotechnol.* **2003**, *21*, 1347–1355.
 - (59) Demandolx, D.; Davoust, J. Multicolour Analysis and Local Image Correlation in Confocal Microscopy. *J. Microsc.* **1997**, *185* (1), 21–36.
 - (60) Anderson, M.; Motta, R.; Chandrasekar, S.; Stokes, M. Proposal for a Standard Default Color Space for the Internet—SRGB. *Color Imaging Conf.* **1996**, 238–245.

- (61) Cromey, D. W. Digital Images Are Data: And Should Be Treated as Such. In *Cell Imaging Techniques. Methods in Molecular Biology (Methods and Protocols)*, vol 931,; Humana Press, 2013; pp 1–27.
- (62) Bolte, S.; Cordelières, F. P. A Guided Tour Into Subcellular Colocalization Analysis in Light Microscopy. *J. Microsc.* **2006**, 224 (3), 213–232.
- (63) Schindelin, J.; Arganda-Carreras, I.; Frise, E.; Kaynig, V.; Longair, M.; Pietzsch, T.; Preibisch, S.; Rueden, C.; Saalfeld, S.; Schmid, B.; et al. Fiji: An Open-Source Platform for Biological-Image Analysis. *Nat. Methods* **2012**, 9 (7), 676–682.
- (64) Miettinen, M. S. Molecular Dynamics Simulation Trajectory of a Fully Hydrated DMPC Lipid Bilayer [Data set]. <https://doi.org/10.5281/zenodo.51635>.
- (65) Tinevez, J. Y.; Perry, N.; Schindelin, J.; Hoopes, G. M.; Reynolds, G. D.; Laplantine, E.; Bednarek, S. Y.; Shorte, S. L.; Eliceiri, K. W. Trackmate: An Open and Extensible Platform for Single-Particle Tracking. *Methods* **2017**, 115, 80–90.
- (66) Sergeeva, E. A.; Katichev, A. R.; Kirillin, M. Y. Two-Photon Fluorescence Microscopy Signal Formation in Highly Scattering Media: Theoretical and Numerical Simulation. *Quantum Electron.* **2010**, 40 (12), 1053–1061.
- (67) Preza, C.; Snyder, D. L.; Conchello, J.-A. Theoretical Development and Experimental Evaluation of Imaging Models for Differential-Interference-Contrast Microscopy. *J. Opt. Soc. Am. A* **1999**, 16, 2185–2199.
- (68) Preza, C. Simulating Structured-Illumination Microscopy in the Presence of Spherical Aberrations. *Proc. SPIE 7904, Three-Dimensional Multidimens. Microsc. Image Acquis. Process. XVIII*, **2011**, 79040D.
- (69) Shterman, D.; Gjonaj, B.; Bartal, G. Experimental Demonstration of Multi Moiré Structured Illumination Microscopy. *ACS Photonics* **2018**, 5, 1898–1902.
- (70) Uster, P. S.; Pagano, R. E. Resonance Energy Transfer Microscopy: Observations of Membrane-Bound Fluorescent Probes in Model Membranes and in Living Cells. *J. Cell Biol.* **1986**, 103 (4), 1221–1234.
- (71) Corry, B.; Hurst, A. C.; Pal, P.; Nomura, T.; Rigby, P.; Martinac, B. An Improved Open-Channel Structure of MscL Determined From FRET Confocal Microscopy and Simulation. *J. Gen. Physiol.* **2010**, 136 (4), 483–494.
- (72) Selin, M.; Fogelqvist, E.; Holmberg, A.; Guttman, P.; Vogt, U.; Hertz, H. M. 3D Simulation of the Image Formation in Soft X-Ray Microscopes. *Opt. Express* **2014**, 22 (25), 30756–30768.
- (73) Noji, H.; Yasuda, R.; Yoshida, M.; Kinosita Jr, K. Direct Observation of the Rotation of F1-ATPase. *Nature* **1997**, 386 (6622), 299–302.
- (74) Veatch, S. L.; Keller, S. L. Separation of Liquid Phases in Giant Vesicles of Ternary Mixtures of Phospholipids and Cholesterol. *Biophys. J.* **2003**, 85 (5), 3074–3083.
- (75) Sage, D.; Neumann, F. R.; Hediger, F.; Gasser, S. M.; Unser, M. Automatic Tracking of Individual Fluorescence Particles: Application to the Study of Chromosome Dynamics. *IEEE Trans. Image Process.* **2005**, 14 (9), 1372–1383.
- (76) Hunter, J. D. Matplotlib : A 2D Graphics Environment. *Comput. Sci. Eng.* **2007**, 9, 90–95.
- (77) Smith, A. R. Color Gamut Transforma Pairs. *Proc. 5th Annu. Conf. Comput. Graph. Interact. Tech.* **1978**, 12–19.
- (78) Abraham, M. J.; Murtola, T.; Schulz, R.; Páll, S.; Smith, J. C.; Hess, B.; Lindah, E. GROMACS: High Performance Molecular Simulations Through Multi-Level Parallelism From Laptops to Supercomputers. *SoftwareX* **2015**, 1–2, 19–25.
- (79) Tironi, I. G.; Sperb, R.; Smith, P. E.; van Gunsteren, W. F. A Generalized Reaction Field

- Method for Molecular Dynamics Simulations. *J. Chem. Phys.* **1995**, *102* (13), 5451–5459.
- (80) Yesylevskyy, S. O.; Schäfer, L. V.; Sengupta, D.; Marrink, S. J. Polarizable Water Model for the Coarse-Grained MARTINI Force Field. *PLoS Comput. Biol.* **2010**, *6* (6), e1000810.
- (81) Verlet, L. Computer “Experiments” on Classical Fluids. I. Thermodynamical Properties of Lennard-Jones Molecules. *Phys. Rev.* **1967**, *159* (1), 98–103.
- (82) Bussi, G.; Donadio, D.; Parrinello, M. Canonical Sampling Through Velocity Rescaling. *J. Chem. Phys.* **2007**, *126* (1), 014101.
- (83) Lindahl, E.; Hess, B.; van der Spoel, D. GROMACS 3.0: A Package for Molecular Simulation and Trajectory Analysis. *J. Mol. Model.* **2001**, *7*, 306–317.
- (84) Cloizeaux, J. Des; Jannink, G. Standard Continuous Model and Perturbation Calculations. In *Polymers in Solution Their Modelling and Structure*; Oxford University Press, **1990**; pp 354–430.

Table of Contents Graphic

